Engineering 3 (2017) 675–684

Contents lists available at ScienceDirect

Engineering

journal homepage: www.elsevier.com/locate/eng

Research
Additive Manufacturing—Article

A Multiscale Understanding of the Thermodynamic and Kinetic Mechanisms of Laser Additive Manufacturing

Dongdong Gu [a,b,*], Chenglong Ma [a,b], Mujian Xia [a,b], Donghua Dai [a,b], Qimin Shi [a,b]

[a] College of Material Science and Technology, Nanjing University of Aeronautics and Astronautics, Nanjing 210016, China
[b] Institute of Additive Manufacturing (3D Printing), Nanjing University of Aeronautics and Astronautics, Nanjing 210016, China

ARTICLE INFO

Article history:
Received 26 March 2017
Revised 15 July 2017
Accepted 28 August 2017
Available online 25 October 2017

Keywords:
Additive manufacturing
Selective laser melting
Multiscale modeling
Thermodynamics
Kinetics

ABSTRACT

Selective laser melting (SLM) additive manufacturing (AM) technology has become an important option for the precise manufacturing of complex-shaped metallic parts with high performance. The SLM AM process involves complicated physicochemical phenomena, thermodynamic behavior, and phase transformation as a high-energy laser beam melts loose powder particles. This paper provides multiscale modeling and coordinated control for the SLM of metallic materials including an aluminum (Al)-based alloy (AlSi10Mg), a nickel (Ni)-based super-alloy (Inconel 718), and ceramic particle-reinforced Al-based and Ni-based composites. The migration and distribution mechanisms of aluminium nitride (AlN) particles in SLM-processed Al-based nanocomposites and the *in situ* formation of a gradient interface between the reinforcement and the matrix in SLM-processed tungsten carbide (WC)/Inconel 718 composites were studied in the microscale. The laser absorption and melting/densification behaviors of AlSi10Mg and Inconel 718 alloy powder were disclosed in the mesoscale. Finally, the stress development during line-by-line localized laser scanning and the parameter-dependent control methods for the deformation of SLM-processed composites were proposed in the macroscale. Multiscale numerical simulation and experimental verification methods are beneficial in monitoring the complicated powder-laser interaction, heat and mass transfer behavior, and microstructural and mechanical properties development during the SLM AM process.

1. Introduction

Additive manufacturing (AM), also widely referred to as three-dimensional (3D) printing (3DP) technology, is based on the philosophy of near-net shaping and freeform fabrication [1–3]. Laser-based AM/3DP technologies, including powder-bed-based selective laser melting (SLM) and powder-feeding-based laser metal deposition (LMD), have been widely applied to manufacture complex-shaped structural/functional metallic parts such as aerospace and gas turbine components [4], biomedical implant components [5], and molds and tools [6]. Due to its application of a fine-focused laser beam and a thin powder layer thickness, SLM is one of the most prevailing AM/3DP technologies and demonstrates a high capability to produce parts with elaborate structures including thin walls, fine features, and small internal channels. With its combination of direct rapid production and high-precision manufacturing characteristics, SLM has received considerable research and application interest around the world [7,8].

Nevertheless, SLM processing of metallic parts involves complicated heat, mass, and momentum transfer within a laser-induced molten pool, resulting in a significant challenge for the fabrication of high-performance SLM-processed components [9–11]. Strict quality-control measures are therefore required in order to ensure the processability, integrity, and performance of SLM-processed components; such measures rely on advanced characterization methods and on a large quantity of processing experiments [12–14]. Matthews et al. [15] disclosed the melt track progression and powder movement under the influence of the hot vapor Bernoulli effect

* Corresponding author.
E-mail address: dongdonggu@nuaa.edu.cn

http://dx.doi.org/10.1016/J.ENG.2017.05.011

by high-speed imaging, thus providing a process control method to control the powder-laser interaction and the resultant melting behavior of the powder. Zhou et al. [16] achieved accurate 3D images of defects inside SLM-fabricated cobalt-chromium-molybdenum (Co-Cr-Mo) samples by using synchrotron radiation micro-computed tomography (CT) imaging, thus expanding the current understanding of the formation mechanisms of metallurgical defects. Zaeh and Branner [17] developed a specific method to evaluate and quantify the residual stresses and deformation due to the temperature gradient mechanism during SLM of tool steel, using finite element (FE) analysis. In order to evaluate structural effects and simultaneously validate a simulation, an analysis of residual stresses based on neutron diffractometry was presented. The monitoring of thermodynamics, kinetics, and thermal stress history during the laser-based AM/3DP process plays an important role in obtaining a tailored process and performance control for layer-by-layer additive manufactured parts. However, as the molten pool during the current SLM process is small and moves quickly on the powder bed, it is difficult to study and monitor the real-time configuration and metallurgical behavior of the molten pool accurately using experimental measures.

In recent years, computational numerical modeling has experienced explosive development as an important tool to deeply understand the underlying physical metallurgical mechanisms during the SLM process for the purpose of quality control [18–20]. In contrast to the computational technologies that have been developed from advanced laser-based welding models, the SLM AM/3DP process involves more complicated physicochemical phenomena (e.g., metal vaporization), thermodynamic behavior, and phase transformation as a high-energy laser beam interacts with loose powder particles. SLM of metals typically involves multiscale coordinated control principles, including microstructure development during SLM processing (the microscale), the laser absorption and melting behavior of powder particles (the mesoscale), and the stress and deformation of SLM-processed structures (the macroscale). In this paper, we provide multiscale modeling and corresponding experimental verification of the SLM processing of metals, alloys, and metal matrix composites, based on a series of previously studied materials in our group, including an aluminum (Al)-based alloy (AlSi10Mg), a nickel (Ni)-based super-alloy (Inconel 718), and ceramic particle-reinforced Al-based and Ni-based composites. The development of multiscale computational numerical simulation and experimental verification methods is beneficial in understanding and monitoring the complicated powder-laser interaction, heat and mass transfer behavior, and development of microstructural and mechanical properties during the SLM AM process.

2. Mesoscale understanding of powder-laser interaction and melting thermodynamic behavior of alloys

2.1. Laser-melting thermodynamics and balling effect control of Al-alloy powder

Computational modeling can provide an important tool for better understanding physical metallurgical phenomena (e.g., melting, evaporation, and solidification) during the SLM of metallic powder, and can act as a precursor when tailoring experimental procedures. However, previously developed modeling has relied on a number of assumptions and thermodynamic behaviors associated with SLM (e.g., balling, porosity) that were impossible to investigate and understand. Fortunately, mesoscale modeling and simulation have recently been considered as a new, highly flexible method of accurately investigating the thermodynamics of the molten pool, based on the powder scale, by eliminating a majority of the physical assumptions that are prevalent in the previous literature [21,22].

Al-alloys are typically difficult-to-process metals for laser-based AM/3DP, due to the special physical properties of Al, including the considerably low absorptivity of Al to lasers, the high affinity of Al melt to oxygen, and the resultant formation of balling defects during SLM. For the SLM processing of AlSi10Mg Al-alloy powder, a novel mesoscale powder-bed model with the dimensions of 400 μm × 300 μm × 60 μm was established, consisting of randomly packed powder particles, as shown in Fig. 1(a). The powder bed consisted of two phases: The first phase comprised randomly packed metallic powder, and the second phase (i.e., the residual regions within the powder bed) was filled with protecting argon gas. To study the thermal melt flow within the molten pool during SLM, the effects of recoil pressure, the Marangoni effect, and evaporative surface cooling were considered. The improved volume of fluid (VOF) methodology was used to solve the coupling effect of the Navier-Stokes equation, energy conservation equation, continuity equation, and VOF equation, and to trace the evolution of the liquid/gas free interface. The SLM apparatus was independently developed, and mainly consisted of a ytterbium fiber laser with a maximum laser power of 500 W, a spot size of ~70 μm, and a wavelength of (1070 ± 10) nm; an automatic powder deposition device; an inert argon gas protection system; and a process control system. All the verified experiments were conducted using the same apparatus. At a relatively low laser energy density caused by a low laser power and a high scanning speed, the sharply variable temperature distribution and surface tension tended to significantly enhance the capillary instability effect within the molten pool (Fig. 1(b)). The molten liquid under the localized laser beam irradiation thus collected and shrank in the neighboring areas, due to the significant melt flow within the pool (Fig. 1(c)), thereby forming small individual balls after solidification. The balling phenomenon eventually occurred on irregularly shaped tracks at a higher scan speed (Fig. 1(d)) due to excessive shrinkage of the liquid track in both the transverse and radial directions, which was normally termed as “shrinkage-induced balling” [23]. In contrast, when a relatively high laser energy density with a high laser power and a low scanning speed was used, the resultant high operating temperature tended to decrease the surface tension of the molten liquid, thus accelerating the liquid to efficiently spread in neighboring areas (Fig. 1(e)). The molten pool was accordingly presented with a stable configuration, free of any evident defects (Fig. 1(e) and Fig. 1(f)), leading to the formation of a regularly shaped track without significant occurrence of the balling effect (Fig. 1(g)). In general, considerable balling of the Al-alloy powder occurred up to an appropriate size of 183.5 μm under a relative energy density of 125 $J \cdot m^{-1}$; it was subsequently reduced significantly as the applied energy density increased, and finally disappeared at a considerably high energy density of 416.6 $J \cdot m^{-1}$. Therefore, it is reasonable to conclude that the laser processing parameters play a crucial role in controlling the balling effect and surface smoothness during the SLM processing of Al-alloy powder.

2.2. Porosity formation mechanism and SLM densification behavior of Ni-alloy powder

A mesoscale simulation, which is typically in the particle-size scale, provides an opportunity to enhance the laser processability (e.g., high densification level, smooth surface quality), which significantly influences the final performance of SLM-processed composites. The SLM AM/3DP of Inconel 718, which is well known as a promising candidate material for various industrial applications, such as aircraft turbine engines, high-speed airframe parts, and high-temperature bolts for nuclear engineering [24,25], generally requires excellent surface integrity and mechanical performance, and can be realized with the aid of a mesoscale simulation. For SLM at a relatively low laser power, a limited amount of energy penetrated into the powder bed and a low operating temperature

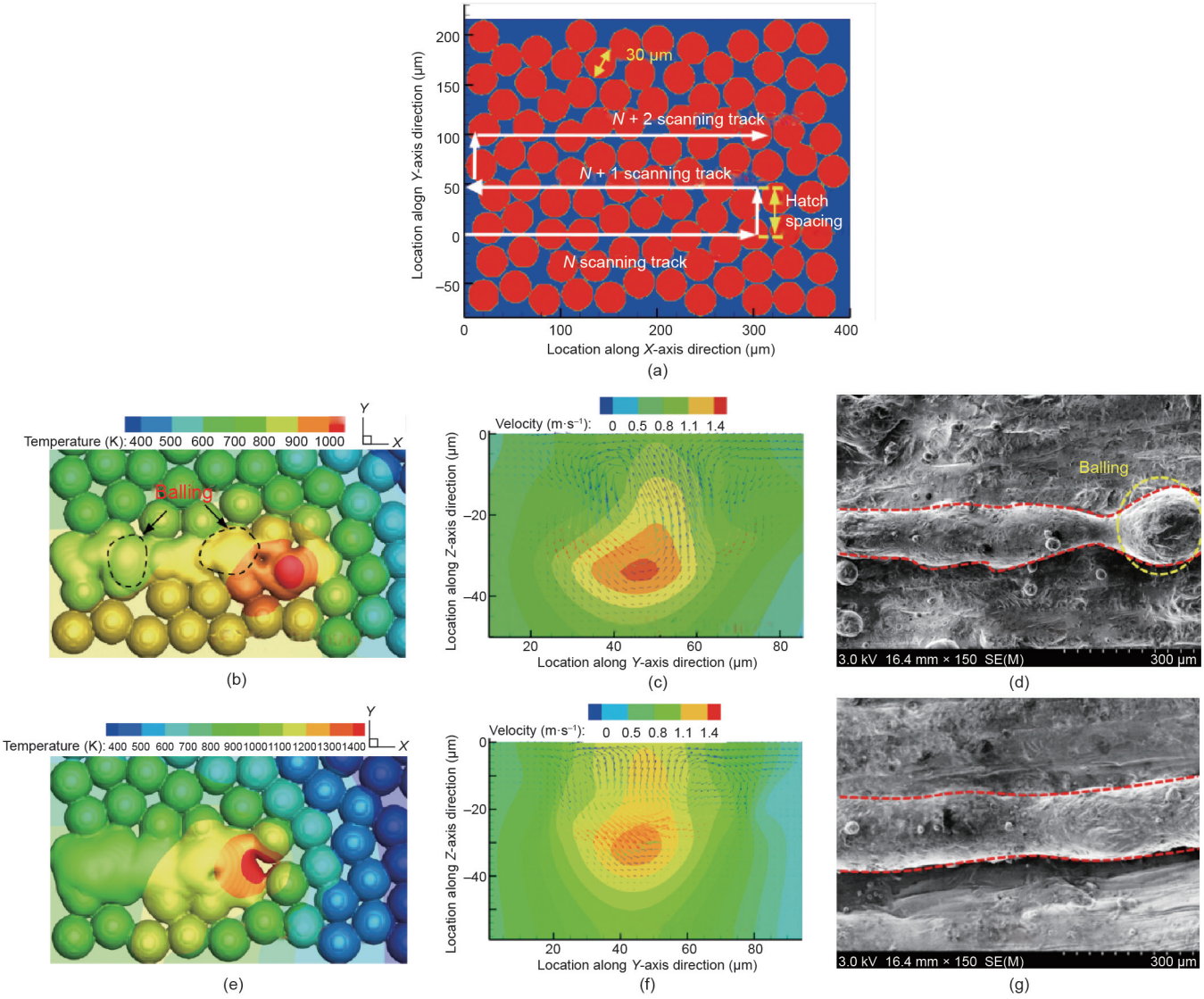

Fig. 1. Thermodynamic behavior of Al-alloy powder during SLM process based on mesoscale analysis. (a) Physical model and scanning strategy used in simulation and experiment; (b) the temperature counters (150 W, 1200 mm·s^{-1}); (c) the velocity counters within the molten pool (150 W, 1200 mm·s^{-1}); (d) the surface morphology of as-built track (150 W, 1200 mm·s^{-1}); (e) the temperature counters (250 W, 600 mm·s^{-1}); (f) the velocity counters within the molten pool (250 W, 600 mm·s^{-1}); (g) the surface morphology of as-built track (250 W, 600 mm·s^{-1}).

was correspondingly generated, resulting in the formation of small molten pools with obvious residual porosity between neighboring pools (Fig. 2(a)). Moreover, the low temperature gradient within the molten pool normally decreased the surface tension of the liquid, which was the primary driving force for the flow of the melt. Under these conditions, the convection within the pool decreased remarkably and, simultaneously, the migration of the melt between the current track and the neighboring solidified track was weakened. As a result, porosity was presented distinctly, both on the cross-section and on the top surface of the SLM-processed composites (Fig. 2(b) and Fig. 2(c)). Conversely, the molten pool exhibited a larger size and was accompanied by a longer liquid lifetime when the applied laser power was increased, due to the considerable laser energy input. The cross-section and top surface of the SLM-processed composites appeared to have a high quality and were free of any obvious defects, due to the intensified convection within the pool and sufficient migration of the melt between the neighboring tracks under the action of a high laser power (Fig. 2(d)–Fig. 2(f)). Moreover, the microstructure surrounding the tracks presented cellular morphology, and no evident defects (e.g., porosity, cracks, etc.) were observed at that time in the neighboring tracks (Fig. 2(g)). According to the results, under the activity of a relatively low power of 90 W, a considerable amount of irregularly shaped porosity with a maximum size of 275.2 μm formed within the neighboring tracks, where limited mass and heat transfer occurred. When the applied power was increased, less porosity exhibiting with the dimension of several microns was generated and was randomly distributed over the surface. Therefore, high-quality Inconel 718 parts with a high surface integrity and densification response are achievable by SLM using reasonable laser processing parameters that can be optimally determined using mesoscale simulation and analysis.

3. Microscale analysis of microstructural development during the SLM of metal matrix composites

3.1. Migration behavior of reinforcing particles within the molten pool during the SLM of Al-matrix nanocomposites

Ceramic particle-reinforced aluminum matrix composites (AMCs), which are one category of high-performance lightweight

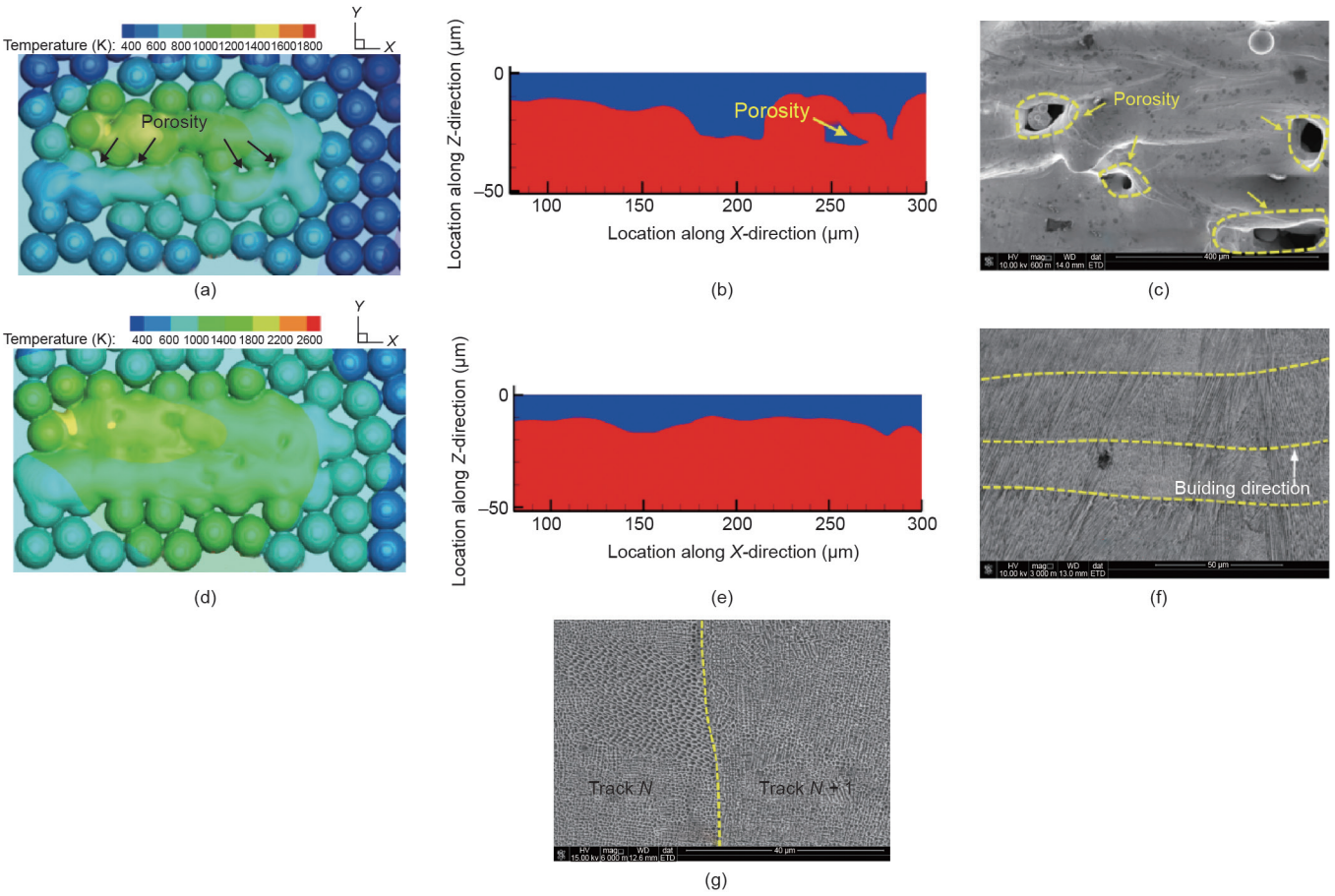

Fig. 2. Tailoring laser processability of Inconel 718 by mesoscale analysis. (a) The temperature counters (90 W, 400 mm·s^{-1}); (b) the cross-sectional quality of as-built layer (90 W, 400 mm·s^{-1}); (c) the top surface morphology of as-built track (90 W, 400 mm·s^{-1}); (d) the temperature counters (120 W, 400 mm·s^{-1}); (e) the cross-sectional quality of as-built layer (120 W, 400 mm·s^{-1}); (f) the top surface morphology of as-built track (120 W, 400 mm·s^{-1}); (g) the high-magnitude microstructure morphology of top surface of as-built tracks (120 W, 400 mm·s^{-1}).

materials, are widely used in aerospace, aircraft, and automotive applications because of their excellent properties, such as high specific stiffness, high specific strength, and excellent wear resistance [26]. Nevertheless, due to the incorporation of hard and brittle ceramic particles with a limited wettability within the Al matrix, simultaneous enhancement of the strength and ductility of AMCs is difficult to achieve. Recent research efforts have revealed that mechanical properties of the AMCs are significantly affected by the particle size of the reinforcement and by the preparation of Al-based nanocomposites; decreasing the size of the ceramic particles to the nanometer level will hopefully lead to a comprehensive improvement of the mechanical properties of AMCs [27]. During the laser-based AM/3DP of nanoparticle-reinforced AMCs, the interaction of the reinforcing particles and the melt within the molten pool play a key role in determining the microstructure evolution of laser-processed composites. Due to the remarkable difference in physical properties between the metal matrix and the reinforcing particles, the particles tend to be pushed by the liquid-solid interface during the laser rapid solidification process, resulting in a non-uniform distribution of reinforcement and in subsequent heterogeneous microstructural and mechanical properties of laser-processed composites. In this section, a 3D transient computational fluid dynamics model is established in order to investigate the influence of processing parameters on the thermal evolution, fluid dynamics, and pressure distribution in the vicinity of the reinforcing particles during the SLM of aluminium nitride (AlN)/AlSi10Mg nanocomposites. The solid-melt coupling mechanism and temperature-dependent thermal physical properties of as-used materials are considered in the numerical model by applying the Gaussian distributed volumetric heat source. The migration behavior of the reinforcing particles within the molten pool is disclosed, in order to achieve a regular distribution of reinforcement in laser-processed AMCs.

Fig. 3 reveals that the melt flow velocity vector near the reinforcement in the melted matrix is highly sensitive to the SLM processing parameters. The surface tension of the Al melt is negatively positive to the operating temperature, meaning that the higher the operating temperature of the irradiation region, the greater the response of the lower surface tension of the Al melt. The thermodynamics and transportation of the AlN reinforcing particles are highly dependent on the melt velocity and operating temperature of the molten pool; the equation of motion and heat transformation is expressed in Ref. [11]. For the AlN/AlSi10Mg composites, the coefficients of the heat conductivity of AlN and AlSi10Mg were ~285 W·(m·K)$^{-1}$ and ~90 W·(m·K)$^{-1}$, respectively, when the operating temperature was above 1000 K. The ratio of the divided thermal conductivities of the reinforcement and metal matrix was equal to 0.3 and, as a result, a concave pattern of the melt convection was generally generated in the neighboring region of the reinforcement. The velocity of the melt convection tended to be significantly enhanced as the melt flowed through the reinforcement (Fig. 3(a) and Fig. 3(b)). Meanwhile, a convection vortex located on one side of the reinforcement was produced as the maximum velocity reached 1.8 m·s^{-1} for a laser energy density of 830 J·mm^{-3} (Fig. 3(c)). As the applied laser energy density further increased to 1000 J·mm^{-3}, a convection vortex with an average velocity of 1.2 m·s^{-1} apparently formed in a symmetrical pattern near the reinforcing particles

(Fig. 3(d)). The convection vortex played a crucial role in the pressure distribution and attendant pressure difference near the reinforcing particles, giving rise to the force acting on the reinforcing particles and the rearrangement of particles. As the applied laser energy density was relatively limited (e.g., η = 550 J·mm^{-3}), the pressure was comparatively uniformly distributed around the reinforcing particles (Fig. 4(a)), and the rearrangement behavior of the reinforcing particles was driven by the combined effect of the

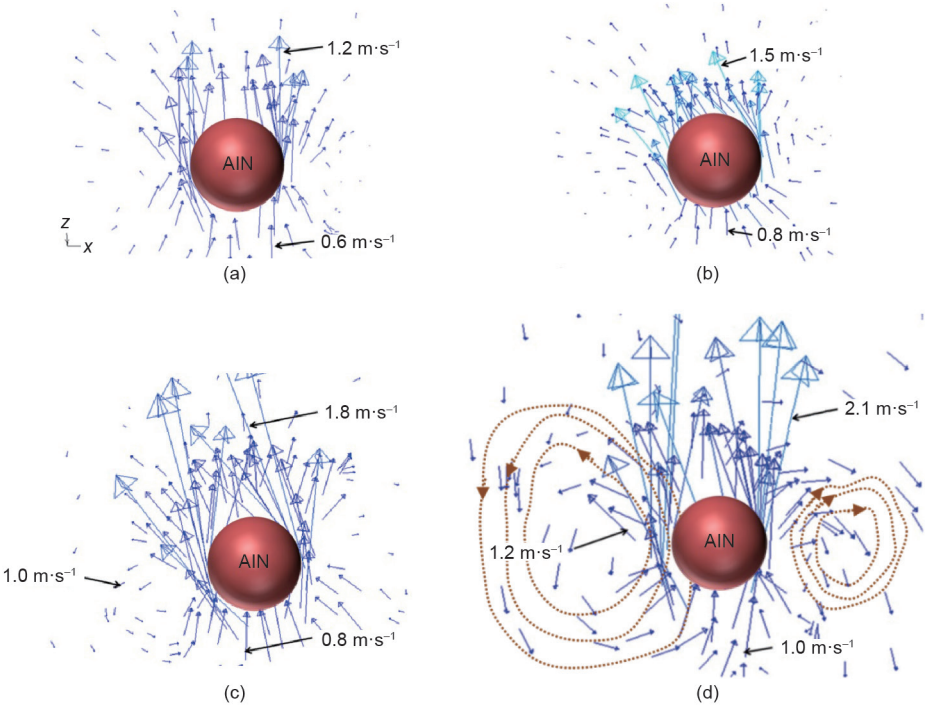

Fig. 3. Characteristics of velocity vector obtained around AlN reinforcing particles using various SLM processing parameters. (a) Laser power P = 100 W, laser energy density η = 550 J·mm^{-3}; (b) P = 130 W, η = 660 J·mm^{-3}; (c) P = 150 W, η = 830 J·mm^{-3}; (d) P = 180 W, η = 1000 J·mm^{-3}.

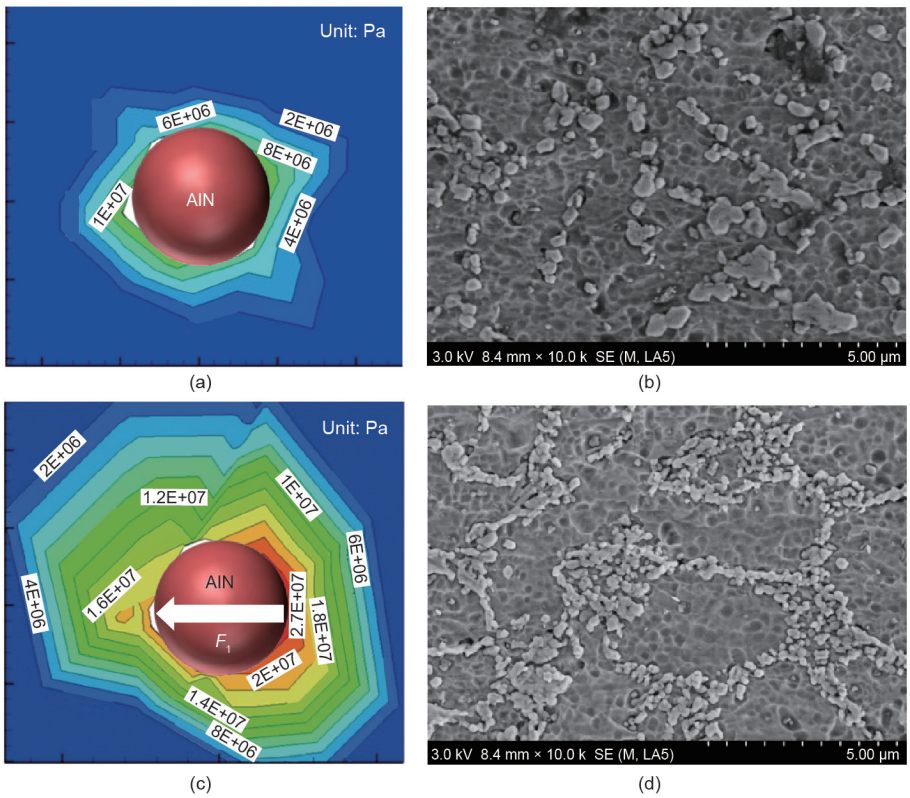

Fig. 4. (a), (c) Pressure distribution in the neighboring region of AlN reinforcing particles and (b), (d) the corresponding distribution state of AlN reinforcing particles within the solidified matrix. (a), (b) Laser power P = 100 W, laser energy density η = 550 J·mm^{-3}; (c), (d) P = 180 W, η = 1000 J·mm^{-3}.

melt convection, capillary force, and gravity force. Therefore, the reinforcing particles have a tendency to be distributed in a random pattern in the solidified matrix (Fig. 4(b)). In contrast, for a high laser energy density of 1000 J·mm^{-3}, the AlN reinforcing particles, driven by the convection vortex and by the forces derived from the pressure difference, tended to migrate in a nearly circular motion, compelled by the centripetal force, F_1 (Fig. 4(c)). As a result, a novel regular distribution of the AlN reinforcing particles in a ring-like shape was obtained within the finally solidified composites (Fig. 4(d)). Therefore, the microscale simulation and understanding of the migration and distribution behavior of reinforcing particles within the laser-induced molten pool are regarded as an efficient way of tailoring the laser processing parameters and realizing a regular distribution of reinforcement in laser-based AM/3DP composite parts.

3.2. Microscale heat transfer behavior of the gradient interface during the SLM of particle-reinforced Ni-based composites

The incorporation of ceramic reinforcing particles into Inconel 718 is an efficient method of improving its high-temperature mechanical performance. However, due to the limited wettability between ceramics and metals and the significant difference in coefficients of thermal expansion, interfacial residual stress and micro-cracks are prone to present themselves. To solve this problem, the gradient interface is tailored between the ceramic reinforcement and the matrix via control of the laser processing parameters and of the *in situ* chemical reaction along the reinforcing particle/matrix interface. The interfacial residual stress, interfacial micropores, and micro-cracks can be controlled and eliminated, hopefully increasing the strength and ductility of laser-formed composites by means of interfacial strengthening.

In order to quantitatively investigate the forming mechanism of the gradient interface within tungsten carbide (WC)/Inconel 718 composites, a 3D numerical model was established [28] that focused on the local thermal performance around the WC reinforcement. Due to the relatively weak capacity of heat transmission of WC in a high-temperature area, the isotherm curves through the reinforcing particle were more intensive than those of the matrix, and the heat flow from the top surface was blocked significantly by the WC particles (Fig. 5(a) and Fig. 5(b)). As a result, annular heat flow was generated around the reinforcing particle and the temperature gradient formed in a radiative fashion from the particle to the matrix (Fig. 5(b)). This accordingly led to the development of a number of dendrites arranged in a radiative fashion around the WC particles (Fig. 5(c)). Furthermore, the formation of an *in situ* gradient interface between the reinforcing particles and the matrix was clearly observable (Fig. 5(d)). The reinforcing particles had spherical morphology and the corners of the particles melted during SLM processing, which was attributed to the local heat accumulation of the WC particles (Fig. 5(b)). A gradient interface with a mean thickness of 0.26 μm formed between the WC particles and the matrix (Fig. 5(d)), preventing the formation of interfacial micro-cracks or micropores. In order to study the chemical composition of the *in situ* gradient interface, an energy dispersive X-ray (EDX) spectroscope analysis was performed at Point A in Fig. 5(d), showing that 73.49 atom% carbon (C) and 11.67 atom% tungsten (W) from the WC particles and 6.66 atom% Ni, 4.81 atom% Cr, and 3.37 atom% iron (Fe) from the Inconel 718 matrix were detected in the gradient interface. The atomic ratio of C and metallic elements was close to 3:1 (73.49 atom% vs. 26.51 atom%). Therefore, it was reasonable to conclude that there was an *in situ* chemical reaction between the reinforcing particles and the matrix, producing a gradient interface with (W, M)C_3 (M = Ni, Cr, Fe) carbide. It was believed that the annular heat flow and radiated temperature gradient around the particle played a key role in promoting the *in situ* interfacial reaction within the molten pool during the SLM of WC/Inconel 718 composites.

Fig. 6(a) and Fig. 6(b) further illustrate the temperature, temperature gradient, and cooling rate at the interface between the reinforc-

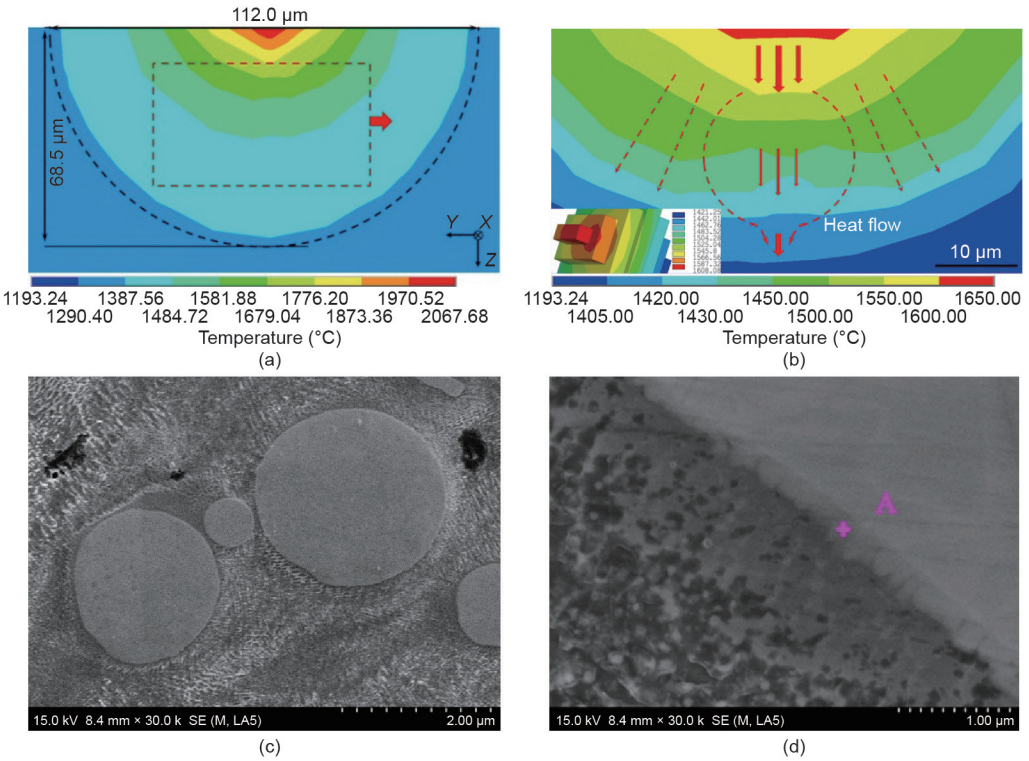

Fig. 5. Numerical simulation results showing the (a) temperature field and (b) heat flow around the reinforcing particle (the bottom-left illustration in Fig. 5(b) showing local heat accumulation of particle); scanning electron microscope (SEM) images showing microstructure of (c) a radiative fashion around the WC particles and (d) tailored gradient interface of SLM-processed WC/Inconel 718 composites at laser power P = 125 W and scanning speed v = 100 mm·s^{-1}.

ing particles and the matrix. A relatively high temperature gradient of 6×10^3 °C·mm^{-1} and a rapid-transition cooling rate of 9.26% were found at the interface. The formation of the gradient interface significantly reduced the tendency of crack and pore formation and improved the bonding coherence at the interface. EDX line-scanning results showed the metallic element distribution along the arrow in Fig. 6(c). It was apparent that from the matrix to the particle, the content of the W element increased, while the contents of the Ni, Cr, and Fe elements decreased. This decreasing tendency was most apparent at the interface (Fig. 6(d)). Fig. 6(e) describes the formation mechanism of the tailored gradient interface in SLM-processed WC/Inconel 718 composites. During the SLM process, the WC and Inconel 718 powder suffered irradiation from the high-energy laser beam, which produced a mobile molten pool (with a width of 112.0 μm and a depth of 68.5 μm, as shown in Fig. 5(a)). Under the impact of local heat accumulation, the WC particles underwent a localized surface melting due to a relatively high melting point, and some W and C atoms were released from the surface into the molten pool (Fig. 5(b)). The Inconel 718 powder melted completely because of its lower melting point, causing the Ni, Cr, and Fe atoms to diffuse into the molten pool. Both the released C and metallic atoms and the laser energy provided the material and energy conditions for the formation of a gradient interface. With the rapid migration of the high-energy laser beam, a very large undercooling promoted the nucleation and growth of the (W, M)C_3 (M = Ni, Cr, Fe) carbide to form the gradient interface, especially under the impact of local heat accumulation and the intense temperature gradient of 6×10^3 °C·mm^{-1} at the interface. Therefore, the tailored formation of a novel gradient interface between the reinforcing particles and the matrix depends on a microscale understanding of the heat transfer behavior within the molten pool and on the dedicated control of material combinations and laser-based AM/3DP processing parameters. On the other hand, the applied laser power played an important role in determining the mean thickness of the gradient interface that was tailored between the WC particles and the Inconel 718 matrix. With the increase of applied laser power, more energy was

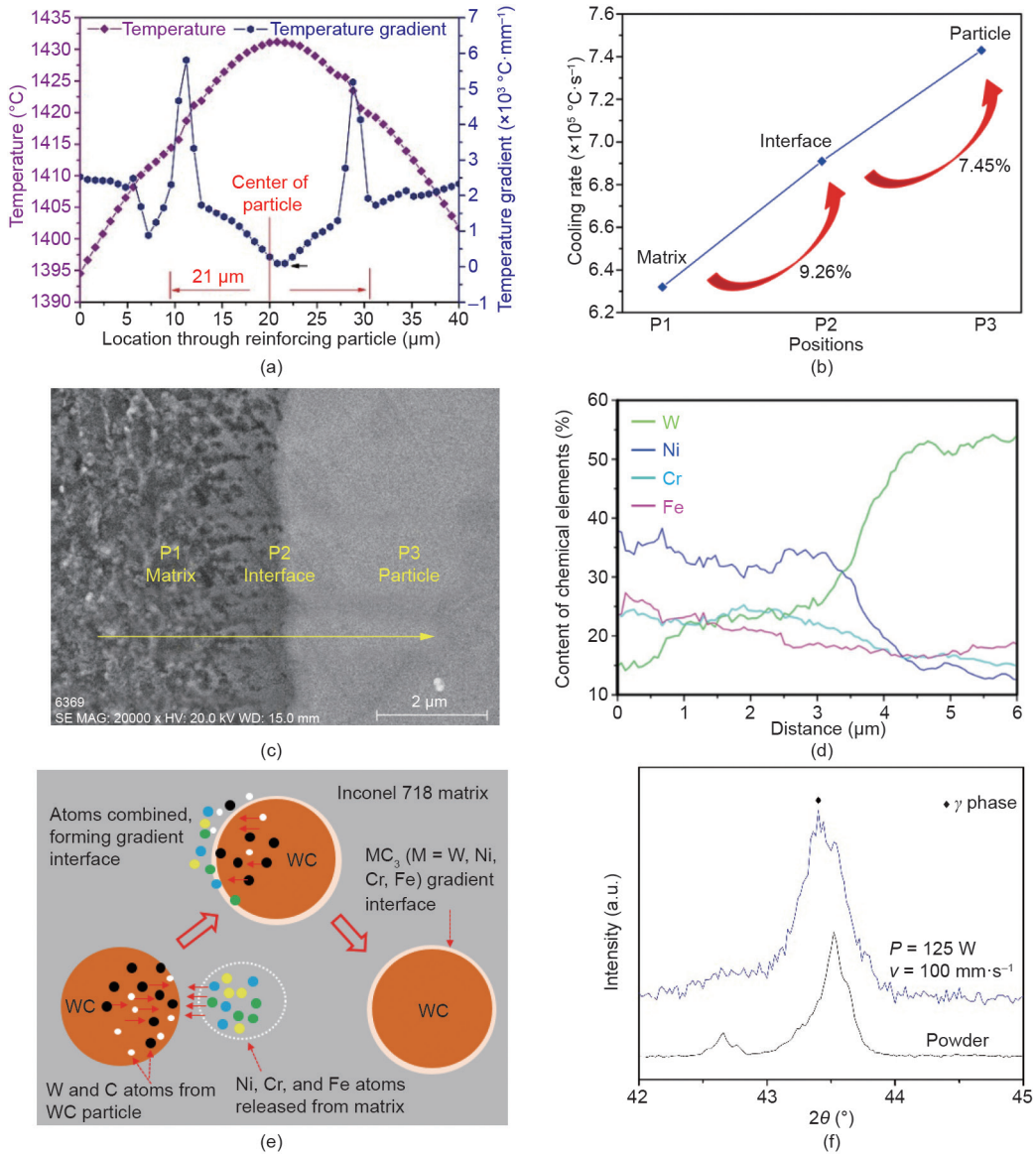

Fig. 6. (a) Temperature and temperature gradient and (b) cooling rate at the interface between the reinforcing particles and the matrix; (c) and (d) EDX line-scanning results showing the metallic element distribution in SLM-processed WC/Inconel 718 composites; (e) the formation mechanism of the tailored gradient interface in SLM-processed WC/Inconel 718 composites; (f) typical X-ray diffraction (XRD) patterns of the primary powder and the SLM-processed WC/Inconel 718 composites obtained in a small range of $2\theta = 42°–45°$.

poured into the molten pool, leading to more W and C atoms being released from the WC particle surface. This provided more material and energy for the shaping of the gradient interface, resulting in a thicker tailored gradient interface. As a result, the mean thickness of the tailored gradient interface was directly proportional to the applied laser power. Typical X-ray diffraction (XRD) patterns of the primary powder and the SLM-processed WC/Inconel 718 composites obtained in a small range of 2θ = 42°–45° are shown in Fig. 6(f). Compared with the 2θ location of the initial powder material, the 2θ location of the diffraction peaks of the γ phase shifted to the lower 2θ. According to Bragg's law:

$$2d \sin\theta = n\lambda \ (n = 1, 2, 3, \ldots) \quad (1)$$

where λ is the wavelength of the X-ray. The observed decrease of 2θ indicated an increase in the lattice between the adjacent lattice planes, d.

4. Macroscale modeling of temperature and stress development and control methods during SLM

For an SLM-processed metallic part at the macroscale, multi-physical thermal behavior and resultant complicated stresses, including thermal stress, contraction stress, and structure stress, are produced during the SLM process, and are regarded as a crucial factor in crack initiation and pore formation. Tracking the thermal stress history is believed to be an efficient way of obtaining more insight into the formation mechanism of structural defects within SLM-processed composites. In this section, an SLM-processed AlSi10Mg Al-alloy part with multi-tracks is taken as an example, and the thermal mechanical coupling effect and residual stress distribution features within the SLM-fabricated part are analyzed.

Fig. 7(a) illustrates the 3D thermo-mechanical coupled FE model, using a Gaussian distributed laser energy density. Based on the nonlinear transient thermal results, a transient stress analysis was conducted with an automatic exchange from a thermal to structural element type, by applying the thermal loadings to the mechanical analysis. The AlSi10Mg powder layer had the dimensions of 1.40 mm × 0.28 mm × 0.05 mm and the Q235 steel layer was taken as the substrate, with the dimensions of 1.40 mm × 0.28 mm × 0.20 mm. In order to obtain sufficient calculation accuracy and efficiency, the powder layer part was meshed with a fine size of 0.0175 mm × 0.0175 mm × 0.0250 mm and the substrate was meshed using a hexahedron element structure. Three different laser scan tracks corresponding to Paths n, n + 1, and n + 2 were marked on the top surface of the powder layer. The variations of temperature and cooling rate of the three target points in the center of the laser scan tracks with the laser beam traveling time are displayed in Fig. 7(b)–Fig. 7(d). Due to the raster scanning mode of the laser beam during SLM, three temperature peaks were observed from the curves; one temperature peak was higher than the AlSi10Mg melting point (660 °C) and the other two were lower than the melting point of AlSi10Mg. For Point 1, the lower temperature peak could act as the annealing effect and, as a result, the stress of Point 1 decreased continuously from 119.26 MPa to 8.68 MPa as the laser beam moved to

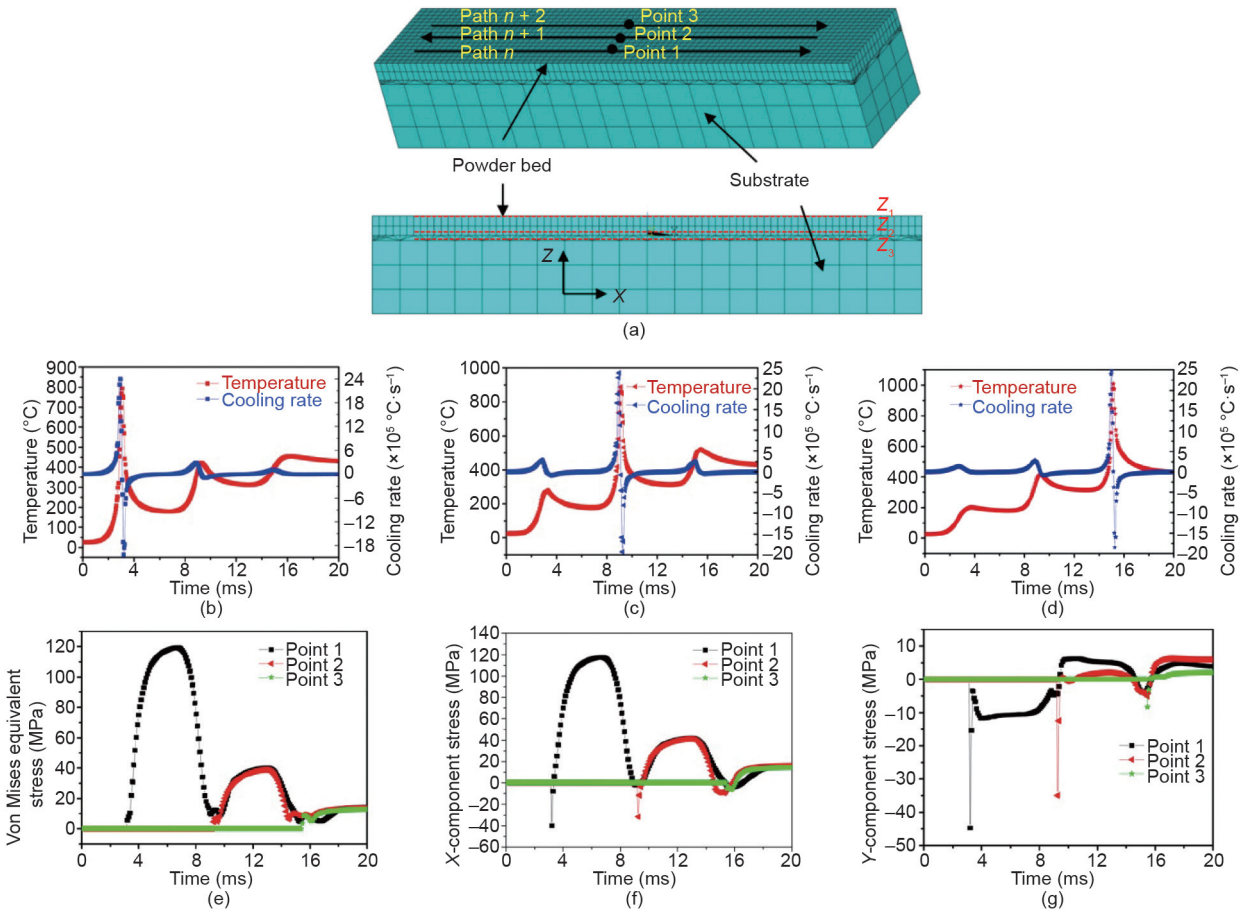

Fig. 7. Variations of temperature and stress developed at the three target points. (a) 3D thermo-mechanical coupled FE model (Point 1, Point 2, and Point 3 locating respectively at the center of laser scan tracks corresponding to Paths n, n + 1, and n + 2 on the top layer); the variations of temperature and cooling rate of (b) Point 1, (c) Point 2, and (d) Point 3 with the laser beam traveling time; (e) von Mises equivalent stress, (f) X-component stress, and (g) Y-component stress of Point 1, Point 2, and Point 3 with the laser beam traveling time.

Point 2 and Point 3 (Fig. 7(e)). For Point 2 or Point 3, the previously obtained lower temperature peaks tended to act as preheating temperatures, leading to a lower initial stress of Point 2 (38.97 MPa) or Point 3 (8.66 MPa) in comparison with that of Point 1. Furthermore, the preheating effect resulted in an increase of the transient temperature peak and a decrease of the cooling rate when the laser beam moved from Point 1 to Point 3 (Fig. 7(b)–Fig. 7(d)). In this situation, Fig. 7(e)–Fig. 7(g) revealed that two different stress components—tensile stress and compressive stress—were found in the stress-time curves. According to the material's states during the SLM process, tensile stress mainly occurred due to uneven contraction of the different solidified regions, while the formation of compressive stress was attributed to the thermal expansion effect of the heated materials.

Due to the localized heating feature of the laser scanning tracks, the difference in the thermal cycles of the laser-induced melting at different regions of the tracks was significant, thereby giving rise to non-uniform residual stress distributions within the SLM-fabricated tracks and layers due to the thermal mechanical coupling effect. In addition, the solidifying rates vary at different regions within the molten pool, in view of different heat transfer features, which further aggravates the local inhomogeneity of the stress distribution. Fig. 8 depicts the *Z*-component residual stress distributions along the Z_1, Z_2, and Z_3 paths (Fig. 7(a)) under different laser energy densities. It was clear that the *Z* component of the residual stress located at the start and finish side of the scanning tracks was much lower than that located in other positions of the scanning track on the top surface (i.e., along the Z_1 path). In contrast, at the bottom of the scanning layer (i.e., along the Z_3 path), the *Z* component of the residual stress located at the start and finish side of the scanning track increased to the maximum values. As a result, the displacement of the edge region at the bottom of the scanning layer was much larger than that of the center region. Meanwhile, on the top of the scanning layer, the displacement of the center region was considerably larger than that of the edge region. When the layer began to be fabricated, the melt located at the upper region and the boundary region of the layer preferentially solidified, taking into account the contact with the cool substrate and the air. As a result, the end of the as-fabricated layer was prone to deformation due to the great solidified stress and shrinkage stress. Subsequently, along the scanning direction of the tracks (in the *X* direction), heat was transferred forward continuously, efficiently decreasing the temperature gradient between the layer and substrate and improving the interface binding. Moreover, along the building direction of the layers (in the *Z* direction), the solidified element located at the boundary region experienced a stronger constraining effect than that located at the upper region, and thus displayed a larger residual stress state. The different distributions of stresses in the different positions along the scanning direction of the tracks (in the *X* direction) and the building direction of the layers (in the *Z* direction) resulted in the formation of interlayer pores and buckling deformation. A reasonable increase in the applied laser energy density tended to decrease the *Z* component of the residual stress, which indicated that the laser energy input played a non-critical role in relieving the buckling deformation of the SLM-processed composites.

5. Conclusions

Multiscale computational numerical modeling has become an essential tool in predicting the thermodynamic and kinetic mechanisms of the SLM AM/3DP process, and thereby efficiently shortening the process optimization cycle of SLM-fabricated parts. In addition, the quantitative data acquired from the numerical modeling provide insight into the scientific problems existing in SLM processing. The basic conclusions of the present study are as follows:

(1) Using mesoscale modeling and simulation, it was determined that for the SLM process of an Al-alloy powder at a relatively high scanning speed or a low laser power, the balling phenomenon, which is a typical metallurgical defect of SLM, tended to occur under the activity of excessive shrinkage of the liquid track in both the transverse and radial directions.

For the SLM of a Ni-alloy powder, when a relatively low laser power was applied, porosity was distinctly presented both on the top surface and on the cross-section of the SLM-processed composites, due to the reduced surface tension of the liquid and the weakened migration of the melt between the current track and the neighboring solidified track.

(2) Using microscale simulation and understanding, it was determined that for the SLM process of AlN/AlSi10Mg nanocomposites, the thermal behavior, thermal-capillary convection, and pressure distribution in the vicinity of the AlN reinforcing particles were sensitive to the SLM processing parameters. Due to the combined effect of the convection vortex, the capillary force, and the gravity force, the pressure difference and centripetal force acted on the AlN reinforcing particle, promoting sufficient rearrangement of the AlN particles. A novel regular distribution of AlN reinforcing particles in a ring-like structure was obtained within the finally solidified composites under the optimized laser energy density. For the SLM of WC/Inconel 718 composites, under the radiation from a high-energy laser beam, an *in situ* chemical reaction occurred between the WC particles and the Inconel 718 matrix, leading to the formation of a gradient interface with (W, M)C_3 (M = Ni, Cr, Fe) carbide. The formation of the gradient interface between the reinforcing particles and the matrix decreased the tendency of crack and pore formation and improved the bonding coherence at the interface.

(3) Using macroscale modeling, the thermal mechanical coupling effect and the residual stress distribution within an SLM-fabricated Al-alloy part were studied. SLM processing of the current track efficiently provided a preheating effect for the un-treated neighboring

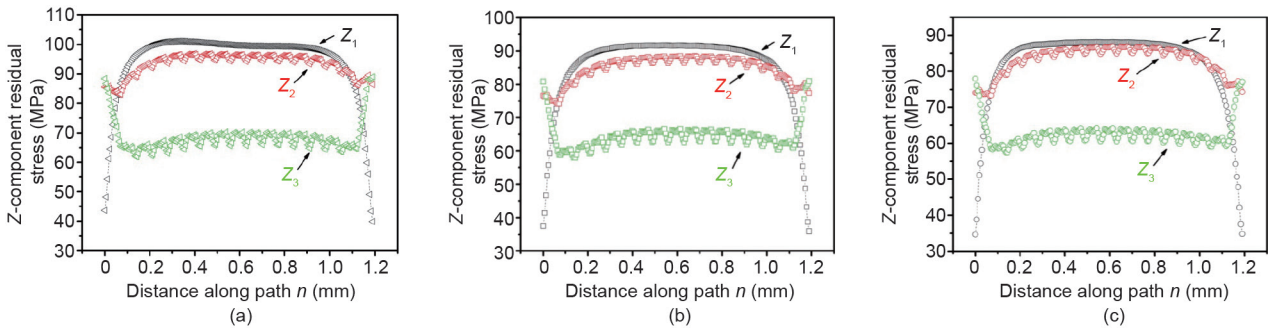

Fig. 8. *Z*-component residual stress distributions of SLM-fabricated parts under different laser energy densities, η. (a) η = 833 J·m^{-1}; (b) η = 1000 J·m^{-1}; (c) η = 1250 J·m^{-1}. Z_1, Z_2, and Z_3 represent three different paths located at various powder layer thicknesses in Fig. 7(a). Z_1 represents the top surface of the layer, Z_2 is 37.5 μm from the top surface, and Z_3 represents the bottom of the layer with 50.0 μm thickness.

powder bed and, meanwhile, provided the annealing effect for the adjacent SLM-processed tracks. The combined effect of self-preheating and self-annealing significantly alleviated the residual stress within SLM parts. The residual stress located at the start and finish sides of the scanning track was much lower than that located in other positions of the track. The residual stress distribution of the SLM-processed layer varied along the depth of the layer. In the bottom of the scanned layer, the residual stress located at the start/finish side increased to the maximum values.

Acknowledgements

The authors gratefully acknowledge the financial support from the National Natural Science Foundation of China (51575267), the National Key Research and Development Program of China "Additive Manufacturing and Laser Manufacturing" (2016YFB1100101), the NSFC-DFG Sino-German Research Project (GZ 1217), the Key Research and Development Program of Jiangsu Provincial Department of Science and Technology of China (BE2016181), and the Aeronautical Science Foundation of China (2015ZE52051).

Compliance with ethics guidelines

Dongdong Gu, Chenglong Ma, Mujian Xia, Donghua Dai, and Qimin Shi declare that they have no conflict of interest or financial conflicts to disclose.

References

[1] Lu BH, Li DC, Tian XY. Development trends in additive manufacturing and 3D printing. Engineering 2015;1(1):85–9.
[2] Derby B. Additive manufacture of ceramics components by inkjet printing. Engineering 2015;1(1):113–23.
[3] Clausen A, Aage N, Sigmund O. Exploiting additive manufacturing infill in topology optimization for improved buckling load. Engineering 2016;2(2):250–7.
[4] Liu Y, Li A, Cheng X, Zhang SQ, Wang HM. Effects of heat treatment on microstructure and tensile properties of laser melting deposited AISI 431 martensitic stainless steel. Mater Sci Eng A 2016;666:27–33.
[5] Haberland C, Elahinia M, Walker JM, Meier H, Frenzel J. On the development of high quality NiTi shape memory and pseudoelastic parts by additive manufacturing. Smart Mater Struct 2014;23(10):104002.
[6] Huang WD, Lin X. Research progress in laser solid forming of high performance metallic components at the State Key Laboratory of Solidification Processing of China. 3D Print Addit Manuf 2014;1(3):156–65.
[7] Wang D, Mai SZ, Xiao DM, Yang YQ. Surface quality of the curved overhanging structure manufactured from 316-L stainless steel by SLM. Int J Adv Manuf Technol 2016;86(1–4):781–92.
[8] Gu DD, Meiners W, Wissenbach K, Poprawe R. Laser additive manufacturing of metallic components: Materials, processes and mechanisms. Int Mater Rev 2012;57(3):133–64.
[9] King W, Anderson AT, Ferencz RM, Hodge NE, Kamath C, Khairallah SA. Overview of modelling and simulation of metal powder bed fusion process at Lawrence Livermore National Laboratory. Mater Sci Technol 2015;31(8):957–68.
[10] Qiu CL, Panwisawas C, Ward M, Basoalto HC, Brooks JW, Attallah MM. On the role of melt flow into the surface structure and porosity development during selective laser melting. Acta Mater 2015;96:72–9.
[11] Dai DH, Gu DD. Influence of thermodynamics within molten pool on migration and distribution state of reinforcement during selective laser melting of AlN/AlSi10Mg composites. Int J Mach Tool Manuf 2016;100:14–24.
[12] Gussone J, Garces G, Haubrich J, Stark A, Hagedorn YC, Schell N, et al. Microstructure stability of γ-TiAl produced by selective laser melting. Scripta Mater 2017;130:110–3.
[13] Kenel C, Grolimund D, Fife JL, Samson VA, Van Petegem S, Van Swygenhoven H, et al. Combined *in situ* synchrotron micro X-ray diffraction and high-speed imaging on rapidly heated and solidified Ti-48Al under additive manufacturing conditions. Scripta Mater 2016;114:117–20.
[14] Kempen K, Thijs L, Van Humbeeck J, Kruth JP. Processing AlSi10Mg by selective laser melting: Parameter optimisation and material characterization. Mater Sci Technol 2015;31(8):917–23.
[15] Matthews MJ, Guss G, Khairallah SA, Rubenchik AM, Depond PJ, King WE. Denudation of metal powder layers in laser powder bed fusion processes. Acta Mater 2016;114:33–42.
[16] Zhou X, Wang DZ, Liu XH, Zhang DD, Qu SL, Ma J, et al. 3D-imaging of selective laser melting defects in a Co–Cr–Mo alloy by synchrotron radiation micro-CT. Acta Mater 2015;98:1–16.
[17] Zaeh MF, Branner G. Investigations on residual stresses and deformations in selective laser melting. Product Eng 2010;4(1):35–45.
[18] Yan WT, Ge WJ, Smith J, Lin S, Kafka OL, Lin F, et al. Multi-scale modeling of electron beam melting of functionally graded materials. Acta Mater 2016;115:403–12.
[19] Gu DD, Yuan PP. Thermal evolution behavior and fluid dynamics during laser additive manufacturing of Al-based nanocomposites: Underlying role of reinforcement weight fraction. J Appl Phys 2015;118(23):233109.
[20] Khairallah SA, Anderson AT, Rubenchik A, King WE. Laser powder-bed fusion additive manufacturing: Physics of complex melt flow and formation mechanisms of pores, spatter, and denudation zones. Acta Mater 2016;108:36–45.
[21] Yu GQ, Gu DD, Dai DH, Xia MJ, Ma CL, Chang K. Influence of processing parameters on laser penetration depth and melting/re-melting densification during selective laser melting of aluminum alloy. Appl Phys A 2016;122:891.
[22] Dai DH, Gu DD. Effect of metal vaporization behavior on keyhole-mode surface morphology of selective laser melted composites using different protective atmospheres. Appl Surf Sci 2015;355:310–9.
[23] Gu DD, Shen YF. Balling phenomena during direct laser sintering of multi-component Cu-based metal powder. J Alloys Compd 2007;432(1–2):163–6.
[24] Zhao XM, Chen J, Lin X, Huang WD. Study on microstructure and mechanical properties of laser rapid forming Inconel 718. Mater Sci Eng A 2008;478(1–2):119–24.
[25] Liang YJ, Li A, Cheng X, Pang XT, Wang HM. Prediction of primary dendritic arm spacing during laser rapid directional solidification of single-crystal nickel-base superalloys. J Alloys Compd 2016;688(Part A):133–42.
[26] Gu DD. Materials creation adds new dimensions to 3D printing. Sci Bull 2016;61(22):1718–22.
[27] Han QQ, Setchi R, Evans SL. Synthesis and characterisation of advanced ball-milled Al-Al_2O_3 nanocomposites for selective laser melting. Powder Technol 2016;297:183–92.
[28] Shi QM, Gu DD, Xia MJ, Cao SN, Rong T. Effects of laser processing parameters on thermal behavior and melting/solidification mechanism during selective laser melting of TiC/Inconel 718 composites. Opt Laser Technol 2016;84:9–22.